PAPER

An automated method for accurate vessel segmentation

IOP Publishing | Institute of Physics and Engineering in Medicine Physics in Medicine & Biology

Phys. Med. Biol. **62** (2017) 3757–3778 https://doi.org/10.1088/1361-6560/aa6418

An automated method for accurate vessel segmentation

Xin Yang[1,4], Chaoyue Liu[1], Hung Le Minh[1], Zhiwei Wang[1], Aichi Chien[2] and Kwang-Ting (Tim) Cheng[3]

[1] Huazhong University of Science and Technology, Wuhan, 430074, People's Republic of China
[2] University of California, Los Angeles, Medical School, Los Angeles, 90095-7350, United States of America
[3] Hong Kong University of Science and Technology, Hong Kong, People's Republic of China

E-mail: xinyang2014@hust.edu.cn

Received 10 October 2016, revised 4 February 2017
Accepted for publication 2 March 2017
Published 6 April 2017

Abstract

Vessel segmentation is a critical task for various medical applications, such as diagnosis assistance of diabetic retinopathy, quantification of cerebral aneurysm's growth, and guiding surgery in neurosurgical procedures. Despite technology advances in image segmentation, existing methods still suffer from low accuracy for vessel segmentation in the two challenging while common scenarios in clinical usage: (1) regions with a low signal-to-noise-ratio (SNR), and (2) at vessel boundaries disturbed by adjacent non-vessel pixels. In this paper, we present an automated system which can achieve highly accurate vessel segmentation for both 2D and 3D images even under these challenging scenarios. Three key contributions achieved by our system are: (1) a *progressive contrast enhancement* method to adaptively enhance contrast of challenging pixels that were otherwise indistinguishable, (2) a *boundary refinement* method to effectively improve segmentation accuracy at vessel borders based on Canny edge detection, and (3) a *content-aware region-of-interests (ROI) adjustment* method to automatically determine the locations and sizes of ROIs which contain ambiguous pixels and demand further verification. Extensive evaluation of our method is conducted on both 2D and 3D datasets. On a public 2D retinal dataset (named DRIVE (Staal 2004 *IEEE Trans. Med. Imaging* **23** 501–9)) and our 2D clinical cerebral dataset, our approach achieves superior performance to the state-of-the-art methods including a vesselness based method (Frangi 1998 *Int. Conf. on Medical Image Computing and Computer-Assisted Intervention*) and an optimally

[4] Author to whom any correspondence should be addressed.

oriented flux (OOF) based method (Law and Chung 2008 *European Conf. on Computer Vision*). An evaluation on 11 clinical 3D CTA cerebral datasets shows that our method can achieve 94% average accuracy with respect to the manual segmentation reference, which is 23% to 33% better than the five baseline methods (Yushkevich 2006 *Neuroimage* **31** 1116–28; Law and Chung 2008 *European Conf. on Computer Vision*; Law and Chung 2009 *IEEE Trans. Image Process.* **18** 596–612; Wang 2015 *J. Neurosci. Methods* **241** 30–6) with manually optimized parameters. Our system has also been applied clinically for cerebral aneurysm development analysis. Experimental results on 10 patients' data, with two 3D CT scans per patient, show that our system's automatic diagnosis outcomes are consistent with clinicians' manual measurements.

Keywords: vessel segmentation, signal-to-noise ratio, contrast enhancement, circle of Wills, retinal vessels, aneurysm development analysis

(Some figures may appear in colour only in the online journal)

1. Introduction

Segmentation of vascular structures is an important task in many medical applications. For instance, for cerebral aneurysm diagnosis and treatment planning, segmenting arteries and their bifurcations in the Circle of Willis, and quantifying their changes over a span of time is a key to facilitate cerebral aneurysm detection and development analysis (Yu *et al* 2015). In diabetic retinopathy (DR) screening, vessels' abnormalities are key symptoms for DR detection and severity classification. In neurosurgical procedures, vessels which give indications of where the blood supply of a lesion is drawn from and drained to serve as landmarks and guidelines to the lesion during surgery.

Technology advancement in medical imaging, such as computed tomography angiography (CTA) and magnetic resonance angiography (MRA), has stimulated explosive growth of medical data. Consequently, automatic vessel segmentation becomes increasingly necessary in order to minimize laborious manual operations and inter-/intra-variability in manual segmentation among clinicians, and in turn to facilitate more efficient and precise diagnosis. There have been a number of research efforts on automated vessel segmentation over years, each of which has distinct strengths. Approaches proposed in Fridman *et al* (2004) and Volkau *et al* (2005) leverage deformable models for 3D vascular segmentation. Active contour implemented based on the level set technique (Yushkevich *et al* 2006, Hernandez and Frangi 2007, Lauric *et al* 2010, Shang *et al* 2011, Tian *et al* 2014, Yang *et al* 2014, Zhao *et al* 2015) is one of the most popular techniques in this category. A major advantage of active contour is the capability of handling topology changes and adapting to shapes of complex vessel structures, yielding high effectiveness for vessel segmentation. Several efforts have been made for further performance improvement. For instance, Nain *et al* (2004) proposed to utilize a ball measurement as a shape prior to penalize local widening of contours and to maintain the shape elongation. Yushkevich *et al* (2006) developed ITK-SNAP to provide a user-friendly interface and live feedback to facilitate parameter selection of active contours for medical image segmentation. However, both methods require extensive manual parameter tuning to achieve a satisfactory result. In addition, these methods apply a single parameter setting globally to all pixels in the entire image data, yielding sub-optimal performance due to the inhomogeneous intensity and contrast of vessel data. Recent efforts (Yang *et al* 2014) have been made to simplify and

automate the parameter settings to achieve optimized performance for various medical data and different levels of image quality. However, the evolution of a deformable surface depends largely on the image quality; active contour based methods usually fail to accurately extract the entire vessels due to an image's low SNR, random noises, image artifacts and disturbances arising from neighboring non-vessel pixels.

Recently, atlas-based methods have been applied as an efficient tool for cerebral vascular segmentation. An atlas is a combination of original images (i.e. the atlas templates) and the corresponding segmentation labels (i.e. the atlas labels). A registration method is first applied to the atlas templates and a target image, and then the atlas labels are propagated to the target image (Passat *et al* 2005, Pohl *et al* 2007, Cabezas *et al* 2011, Bustamante *et al* 2015). Despite accurate segmentation for the majority of vessel pixels, altas-based methods require massive manual labels and data collection for vessels of various sizes, from aorta or blood capillaries, which is laborious and time consuming. In addition, they often lack the flexibility in local fine tuning of vessel boundaries.

Another category of approaches is based on vessel enhancement filters which assign a filtering score to each individual pixel based on local information around the pixel, the score indicates the likelihood of this pixel being part of a vessel. Based on these response scores, a classifier then assigns each pixel as either a vessel or a non-vessel pixel (Frangi *et al* 1998, Law and Chung 2008, 2009, González *et al* 2009, Rigamonti and Lepetit 2012, Becker *et al* 2013, Rigamonti *et al* 2013, Annunziata *et al* 2015, Wang *et al* 2015a). Several vessel enhancement filters have been developed in recent years. One of the most notable filters is the vesselness filter proposed by Wang *et al* (2015a) based on the Hessian matrix. This filter computes the Hessian matrix for each pixel based on information within a small neighborhood of the pixel. The eigenvalues of the Hessian matrix are used to differentiate among plane-, blob- and tubular-like structures, and the corresponding eigenvectors indicate the vessel orientation at this pixel. A multi-scale strategy is applied in order to detect vessels of different sizes. Rather than relying on the Hessian matrix, several methods proposed to utilize the local distribution of gradient vectors. For instance, Bauer and Bischof (2008) proposed to utilize the eigenvalues of the gradient vectors' covariance matrix for local structure analysis. In Bauer and Bischof (2008), Bauer *et al* replaced the multi-scale computation of the gradient vectors by the gradient vector flow (GVF), and then applied the Frangi's vesselness measure on the GVF to detect the centrelines of vessels. In Law and Chung (2008) the authors proposed to use optimally oriented flux (OOF) (Law and Chung 2008) to detect curvilinear structures such as vessels. OOF relies on the measure of gradient flux through the boundary of local spheres. Compared to the Hessian-based filters, OOF is generally more robust against the disturbances induced by adjacent structures. Recent studies pointed out that real vascular structures do not always conform to an ideal tubular shape model and unconformity to the model can greatly degrade the segmentation accuracy based on handcrafted vessel filters. To address this problem, several methods (Bauer and Bischof 2008, González *et al* 2009, Rigamonti and Lepetit 2012, Becker *et al* 2013, Rigamonti *et al* 2013, Wang *et al* 2015b) have been proposed to learn vessel shapes from a large set of vessel images. For instance, Agam and Wu (2005) proposed probabilistic vessel models which are learned based on eigenvalue analysis of the structure tensor. The learned vessel models can enhance vessel junctions yet suppressing nodules. In a similar fashion, González *et al* (2009) learned rotational features based on steerable filters to represent filaments from a set of training data. Based on these learned rotational features, an SVM classifier assigns pixels as vessel or non-vessel pixels. Experimental results demonstrate that the learned models in González *et al* (2009) can not only detect ideal curvilinear structures but also non-ideal filament structures, some of which, such as junctions, could not be modeled previously. Inspired by González *et al* (2009), a series of enhancements (Rigamonti

and Lepetit 2012, Becker *et al* 2013, Rigamonti *et al* 2013) were made, including adding more filters in addition to the steerable filters for training vessel models, and leveraging more advanced machine learning techniques for vessel versus non-vessel pixels classification. A comprehensive survey of vessel enhancement and segmentation methods can be found in Fraz *et al* (2012) and Kirbas and Quek (2004). However, both handcrafted and learned filters still rely on analysis of image gradients or high-order derivatives (Roychowdhury *et al* 2015) which are usually sensitive to noise. Poor image quality arising from low intensity contrast and low SNRs could result in ambiguous responses for those filters, and in turn yield inaccurate vessel segmentation.

In this study, we develop an automated vessel segmentation system which is based on filter-based methods and primarily focuses on addressing the limitations of existing methods under the following two challenging, and commonly occurred, scenarios: (1) in regions with low contrast and low SNR, and (2) at vessel boundaries which are also very close to non-vessel tissues with similar intensity values to those of vessels'. To this end, this paper makes the following three contributions:

1. A *progressive contrast enhancement* method that focuses on improving visibility of challenging pixels progressively by excluding a subset of pixels, which have been identified as vessel pixels with a high confidence in previous iterations, from contrast enhancement in the subsequent iterations. Compared to existing contrast enhancement methods (Zuiderveld 1994) which process all pixels with equal emphasis within a particular region, the proposed method eliminates the potential disturbance arising from 'known' pixels in each iteration and places more emphasis on the remaining 'unknown' pixels which are difficult to handle and yet to be classified. As a result, our approach can better capture subtle vessel information in low contrast, low SNR regions. To further suppress noises in low SNR regions, we propose *shape-weighed contrast enhancement* to emphasize the contributions of vessel-like pixels and de-emphasize the impact of noises in the contrast enhancement procedure. The idea behind this strategy is based on the complementary characteristics between the shape information and the intensity information and hence the chance of having both large shape responses and intensity values for a non-vessel pixel is much smaller than for a vessel pixel.
2. A *boundary refinement* method which refines segmentation results nearby vessel boundaries based on Canny edge detection. Specifically, Canny edge detection is applied to localize potential vessel boundaries. A verification map is then generated based on the detected edges to determine whether a pixel is between two vessel boundaries or is outside a vessel. False positives which are non-vessel pixels while mis-classified as vessel pixels in the previous step can now be filtered out based on the verification map.
3. A *content-aware ROI adjustment* method which automatically adjusts the locations and sizes of ROIs for further contrast enhancement and verification. In particular, our method checks the continuity and shape consistency of a vessel along the centerline of the segmented vascular structure. Sub-regions encompassing disconnected vessel segments or sudden shape changes are identified as suspicious regions including segmentation errors arising from low contrast and SNR. These regions are hence fed to progressive contrast enhancement module for further processing and verification. Compared to existing contrast enhancement methods (Zuiderveld 1994) which partition an image into equal-sized grids using a pre-determined grid size, our method adaptively adjusts the ROI's location and size according to the content and requirement in each iteration, yielding better enhancement results.

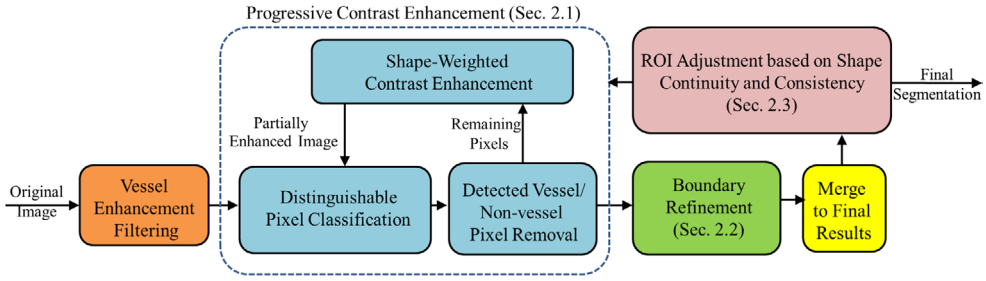

Figure 1. The framework of automated vessel segmentation system, which includes three key components: (1) progressive contrast enhancement, (2) boundary refinement and (3) content-aware ROI adjustment.

We conducted extensive experiments to demonstrate the performance of the proposed system. First, we compared our method with the state-of-the-art filter-based methods: vesselness based method (Frangi *et al* 1998) and the optimally oriented flux (OOF) based method (Law and Chung 2008) on two datasets—a public 2D retinal dataset (i.e. DRIVE (Staal *et al* 2004)) and a 2D clinical cerebral dataset collected by us. Experimental results demonstrate that our approach achieves superior performance to the two methods mentioned above. We then extended our method for 3D segmentation and conducted experiments on 11 clinical 3D CTA datasets, each of which includes a complete Circle of Wills. The results produced by our system matched well, with an average accuracy of 94%, with manual segmentation results, which is 23% to 33% better than the five baseline methods (Frangi *et al* 1998, Yushkevich *et al* 2006, Law and Chung 2008, Wang *et al* 2015a) using manually optimized parameters. Finally, we applied our system for quantitative analysis of cerebral aneurysm development. Experimental results based on 10 patients' data, with two separate 3D CT scans for each patient acquired about six months apart, demonstrated that the diagnosis produced by our system is highly consistent with clinician's manual measurement, exhibiting its great potential for clinical application.

2. Method

Figure 1 illustrates the framework of our vessel segmentation system. Given an input image, conventional vessel enhancement filtering, such as the vesselness or OOF, is first applied to enhance the vessel regions in the image. Three steps are then iteratively employed for progressive contrast enhancement (section 2.1): (1) identifying distinguishable pixels which can be labeled as vessels or non-vessels with a high confidence, (2) removing the identified vessel/non-vessel pixels from the image, and (3) enhancing contrast of the remaining challenging pixels which are difficult to be classified in the current iteration. This process iterates until no more fine-vessel pixels can be detected (i.e. the number of pixels removed in an iteration is sufficiently small) or a limit on the iteration count is reached. After each iteration of progressive contrast enhancement, pixels with labels of a high confidence are further verified by a boundary refinement process (section 2.2), and the pixels which pass the boundary refinement process are included in the segmentation pixel set. After progressive contrast enhancement converges, the candidate set of segmented vessel pixels is obtained. We check each vessel's continuity along the vessel's direction and the consistency of vessel's diameter in a small neighborhood. If there are disconnected vessel segments or sudden changes in a vessel's thickness, the corresponding ROI is considered to encompass suspicious vessel segments and

then sent back to progressive contrast enhancement for further processing and verification. In the following, we provide details of each step.

2.1. Progressive contrast enhancement

Given an input vessel image enhanced after vessel filtering, we first detect distinguishable pixels that can be identified as non-vessels/vessels with a high confidence. Specifically, we set two strict thresholds T_H and T_L. Pixels whose filtering responses are greater than T_H or smaller than T_L are classified as vessel and background pixels respectively. The remaining pixels whose responses fall within the range of T_H and T_L are considered as 'unknown' and their labels will be determined in a later step. T_H and T_L are selected to ensure that over 95% vessel pixels and non-vessel pixels of the training images can be correctly classified respectively. Once pixel classification in this iteration completes, we remove 'known' pixels from further consideration in future iterations. For the remaining 'unknown' pixels, we partition the image into regular-sized grids and for each grid x we generate a normalized histogram of the remaining 'unknown' pixels (i.e. the probability distribution) with a bin for each possible intensity $p_x(i)$:

$$p_x(i) = \frac{\text{number of pixels with intensity } i}{\text{total number of remaining pixels in } x} \quad i = 0, 1, \ldots, L \tag{1}$$

where L is the total number of gray levels in the image (typically 256). To enhance the contrast of each grid, we stretch out the corresponding probability distribution to a wider and more uniform distribution of intensity values according to a transformation function defined as equation (2),

$$T(i) = \text{round}(\text{cdf}_x(i) \times (L - 1)) \tag{2}$$

where $\text{cdf}_x(i)$ is the cumulative distribution function (CDF) defined as equation (3),

$$\text{cdf}_x(i) = \sum_{j=0}^{i} p_x(j), \quad 0 \leqslant i \leqslant L \tag{3}$$

Based on the transformation function, each pixel with intensity i in region x will be mapped to a pixel with intensity $T(i)$ in the histogram equalized region y which has a flat histogram with a linearized CDF across the entire range, for a constant K.

$$\text{cdf}_x(i) = \text{i}K \tag{4}$$

Conventional histogram equalization methods, such as CLAHE, generate intensity distribution based on all pixels within a region. It is common that both small vessels and large vessels exist in a region and the distribution is easily dominated by large vessels which are visually clear in an image and can be easily classified. As a result, the contrast of small vessels cannot be sufficiently enhanced. Reducing the grid size could limit the vessel size differences in a grid and in turn alleviate this problem. However, a small grid size also increases the chance that few vessels exist in a grid and thus contrast enhancement in such a grid over-amplifies noises. Figure 2(a) shows the contrast-enhanced result of a retinal vessel image based on CLAHE. A small region which contains both small vessels and part of a larger vessel is highlighted using

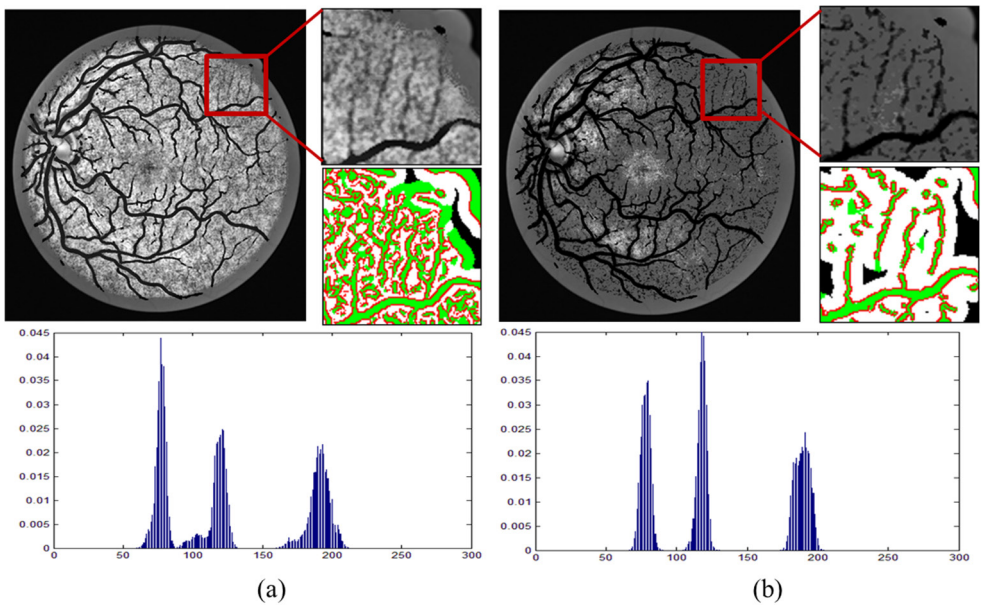

Figure 2. Contrast enhancement results based on (a) CLAHE and (b) the 2nd round progressive contrast enhancement on an exemplar retinal image. A small region including both challenging pixels (i.e. subtle vessels) and part of a larger vessel is denoted by a red rectangle. An enlarged version of the region and the corresponding verification map are displayed on the right. The probability distribution of the original region is displayed underneath. The probability distribution shows that fewer small vessel pixels are within the intensity range of [55, 95] in (b) than in (a), yielding smaller intensity values for small vessels after enhancement and greater intensity differences between small vessels and background. As a result, our progressive contrast enhancement can better improve visibility and obtain a more accurate verification map for small vessels. The parameter settings for CLAHE are the same for both (a) and (b) where the clip limit = 30 and the region size = 50 × 50.

a red rectangle and show the verification map of this region together with its probability distribution before enhancement. From the probability distribution we observed that there are more vessel pixels within the intensity range of [55, 95] in figure 2(a) than in figure 2(b), yielding a greater $\mathrm{cdf}_x(i)$ value at intensity i for figure 2(a) which is the intensity value for small vessels. As a result, small vessels will have a greater intensity value $T(i)$ after enhancement and in turn yield a smaller intensity differences between small vessels and background. In comparison, our method performs enhancement only on 'unknown' pixels, thus more pixels in the fine vessels can be better enhanced and detected. By comparing the enlarged enhanced region and its verification map in figures 2(a) and (b) we can clearly observe that our method can provide much better visibility for small vessels and greatly reduce noises in the verification map. Once some of the remaining pixels can be easily classified with high confidence based on (T_h and T_L), we excluded them for further consideration. Such procedure iterates until no more fine-vessel pixels can be detected or a limit on the iteration count is reached.

Pseudo code 1 Shape-weighted progressive contrast enhancement.

Input: Original image I, vessel enhancement image I_{ve}
Parameters T_h, T_L, λ, grid size $k \times k$
Output: Segmentation result
Procedure: shape-weighted progressive contrast enhancement
Partition $\boldsymbol{I}$ into equal-sized $(k \times k)$ grids $\{X\}$
for $x = \{X\}$ **do**
Initialize $\{P\}$ as all pixels in x
while (!converge) **do**
for $m = \{P\}$ **do**
Update shape-weighted histogram according to equation (5)
end for
Calculate the cumulative distribution function according to equations (3) and (6)
I_{pe} = **Histogram equalization** according to equations (1)–(3)
(I_{pe} is the enhanced image in this iteration)
$[\{P_{\text{vessel}}\}, \{P_{\text{back}}\}]$ = **Pixel classification**(I_{pe}, T_h, T_L)
($[\{P_{\text{vessel}}\}, \{P_{\text{back}}\}]$ are labelled pixels with high confidence)
Remove $\{P_{\text{vessel}}\}, \{P_{\text{back}}\}$ from $\{P\}$
end while
end for

To further improve the progressive enhancement performance, we integrate local geometric structures with the intensity information for normalized histogram construction and equalization. The underlying idea behind is that the local geometric structure around each pixel is a discriminating and complementary feature to the intensity information for differentiating vessel pixels from random noises. Combining the local shape information with intensity can better suppress random noises since for noise pixels the chance of is less likely that noise pixels have having similar values of both shape responses and intensity as vessel pixels is quite small. Based on this idea, we propose to use normalized local shape information $S(x_m)$ obtained from vessel enhancement filtering (e.g. vesselness or OOF) to weight contribution of each pixel to the histogram construction, as shown in equation (5).

$$\text{Hist}(i) += (S(x_m))^{\lambda} \quad 0 \leqslant i \leqslant 256 \tag{5}$$

where x_m is the mth pixel in region x, and λ is used to adjust the impact of the weights. Since we normalize $S(x_m)$ to the range of [0, 1], larger λ results in smaller impact of weighting and vice versa. We tried λ value exhaustively and found that $\lambda = 0.8$ provides the best segmentation accuracy in our training data and hence is used as our default value. The probability distribution can be calculated according to equation (6),

$$p(i) = \frac{\text{Hist}(i)}{\sum_x (S(x_m))^{\lambda}} \tag{6}$$

Pseudo code 1 summarizes the process of our shape-weighted progressive contrast enhancement.

2.2. Boundary refinement

Precisely localizing vessel boundaries is important for quantitative analysis of vessel abnormalities. For instance, to analyze the growth of a cerebral aneurysm, we usually register the aneurysm and surrounding segmented vessels from two CT scans which are acquired at two different times. Then, we calculate the vessel thickness difference and aneurysm volume difference of

(a) (b) (c)

Figure 3. (a) Segmented vessels based on vesselness filtering overlaid with detected canny edges. True positives, false positives and canny edge pixels are denoted by white, red and blue colors respectively. (b) Illustration of the verification map. Pixels reside inside a vessel, outside a vessel and at vessel boundary are denoted by green, white and red colors respectively. (c) Illustration of the verification map construction.

the two scans. Incorrectly localizing vessel boundaries result in errors in estimating the vessel thickness and aneurysm volume, and in turn lead to misdiagnosis. In this study, we develop an effective and robust boundary refinement method based on Canny edge detection. First, we apply Canny (Canny 1986) to localize a set of edge pixels $E = \{E_i | E_i \text{ is an edge pixel }\}$ as potential vessel boundaries. As shown in figure 3(a) where we overlay the detected Canny edges (i.e. the blue pixels) with the vessel segmentation. In the figure, white, red and green pixels indicate true vessel pixels, false vessel pixels and miss detected vessel pixels in the segmentation, respectively. Clearly, most canny edge pixels correctly locate at real vessel boundaries, forming 'classification planes' to exclude false vessel pixels from the true segmentation.

Second, we design a simple yet effective method to construct a verification map for precisely localizing vessel boundaries and excluding false positives (i.e. non-vessel pixels mistakenly classified as vessel pixels with high confidence in the previous step) which are outside a vessel tube and close to vessel boundaries. Specifically, for every non-edge pixel $P \notin E$, we construct two vectors: (1) a vector $\overrightarrow{PE_i}$ pointing from P to a nearby canny edge pixel E_i, and (2) a normalized gradient vector at pixel E_i, i.e. $\frac{\overrightarrow{\text{grad}_{E_i}}}{|E_i|}$. Assuming that vessel pixels are generally darker than the background, the result of the dot product between the two vectors $F_p = \frac{\overrightarrow{\text{grad}_{E_i}}}{|E_i|} \cdot \overrightarrow{PE_i}$ is greater than zero if P locates inside a vessel tube (i.e. the angle between the two vectors are smaller than 90°); otherwise the dot product result is negative (as shown in figure 3(c)). For every edge pixel $P \in E$, the corresponding value of F_p is 0.

A verification map based on a single edge pixel E_i could be sensitive to noises. To improve the robustness, for every pixel P we consider a set of the canny edge pixels $\{E_i \in R\}$ near P and sum up the weighed dot products according to equation (7) (as illustrated in figure 3(c)).

$$F_p = \sum_{E_i \in R} \frac{w_{E_i}}{|E_i|} \left| \overrightarrow{\text{grad}_{E_i}} \cdot \overrightarrow{PE_i} \right|, \tag{7}$$

The range R affects the number of neighboring pixels for computing F_p. In our experiment, it is automatically determined based on the greatest diameter of all segmented vessels in the first iteration. Such setting can guarantee that all true vessel pixels can have at least one edge pixel E for computing F_p. In addition, large vessels with greatest diameter can be easily segmented correctly in the first iteration. The weight w_{E_i} is calculated based on a Gaussian distribution centered at P as shown in equation (8), where (x_P, y_P), (x_{E_i}, y_{E_i}) are coordinates of

pixels P and E_i, and σ is the standard deviation of the Gaussian distribution. Accordingly, edge pixels which are further away from pixel P have a smaller impact on F_p than those closer to P.

$$w_{E_i} = \exp\left(\frac{(x_P - x_{E_i})^2 + (y_P - y_{E_i})^2}{2\sigma^2}\right) \tag{8}$$

The sigma value affects the final segmentation performance. We experimentally tested a range of configurations to search for one which achieves the greatest segmentation accuracy and based on the experimental results we set sigma to 2.5. Based on F_P we can construct a verification map V_p according to equation (9).

$$V_p = \begin{cases} 1 & F_P > 0 \text{ and } P \notin \{E\} \\ 0 & P \in \{E\} \\ -1 & F_P < 0 \text{ and } P \notin \{E\} \\ \text{null} & R_P \cap \{E\} = \varnothing \end{cases} \tag{9}$$

In other words, for each image we can construct a verification map V_p with the same size as the input image and each entry of the map is a value of quadruples $\{1, 0, -1, \text{null}\}$ (as shown in figure 3(b)), where 1 (green) and -1 (white) indicate pixels inside and outside a vessel tube, respectively. A 0 (red) denotes a pixel at the boundary and null (black) indicates pixels far from any edges and thus unnecessary to be examined in the current iteration.

Based on the verification map V_p we can refine the segmentation result at regions which locate outside a vessel tube and are very close to vessel boundaries. Specifically, for every pixel which was identified as a vessel pixel in the previous step while was labeled as -1 on the verification map, we re-classify it as negative (i.e. a non-vessel pixel) and merge it into the final segmentation results. The segmentation result after verification won't be changed unless it violates the shape continuity and consistency rule, as shown in figure 1. It is also possible to re-label the segmentation results for pixels which are labeled as 1 on the verification map while were identified as non-vessel pixels. However, in the specific experiment we conducted, we did not re-label these pixels as we observed that mis-segmentation is primarily caused by false positives (as shown in figure 3(a)), not false negatives. This phenomenon, however, is dependent on the classification thresholds T_H and T_L used in the previous segmentation step. A smaller (larger) T_H (T_L) could result in more false positives (false negatives) and in turn re-labeling either or both of false positives and negatives based on the verification map may become necessary. In practice, if we allow users to tune the T_H and T_L values, the usage of a verification map should be adjusted accordingly to exclude either false positives or false negatives from re-labeling for an optimized performance.

2.3. Content-aware ROI adjustment

Dividing an image into equal-sized grids and applying a predetermined parameter setting to all grids basically ignores image content within a grid for contrast enhancement. For grid regions which contain non-vessel tissues those are spatially close to (or even attached to) vessels and share similar intensity values as vessels, such an approach usually results in insufficient enhancement to separate vessel pixels from non-vessel pixels. Therefore, adaptively adjusting an ROI' size and location according to the image content is necessary for such challenging cases. In this section, we present our content-aware ROI adjustment method to address this problem.

Once progressive contrast enhancement and boundary refinement are completed, we could obtain a candidate set of segmented vessel pixels. For true vessel pixels, they usually obey two rules: (1) they are spatially connected, i.e. one vessel pixel is among the 8 (or 26) neighbors of another vessel pixel in the 2D (or 3D) segmented vessel structure, and (2) the diameter of a vessel's

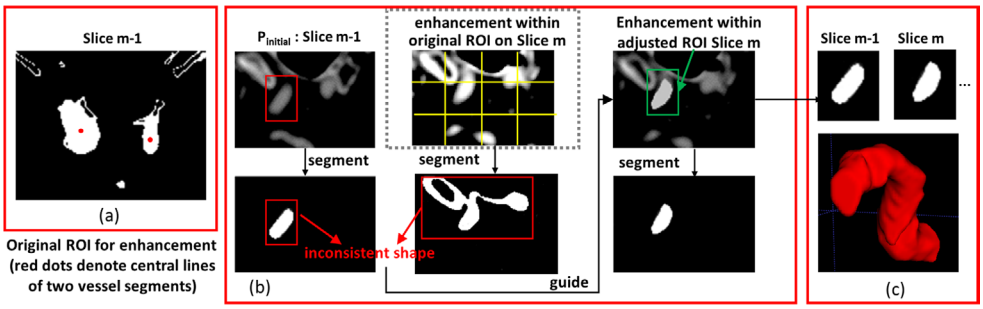

Figure 4. Illustration of ROI adjustment based on shape continuity and consistence (a) Cross section of an original ROI (i.e. grid region x) for enhancement. The red dots denote the central points of two vessel segments. (b) If there is shape inconsistency or spatial disconnectivity detected in an ROI, the size and location of a ROI is adaptively adjusted to encompassing a vessel where the inconsistency and/or disconnectivity occur. The quality of the ROI is improved for further verification and segmentation. The adjusted ROI is propagated for further examination. (c) Segmentation of an internal carotid artery (ICA) based on ROI adjustment.

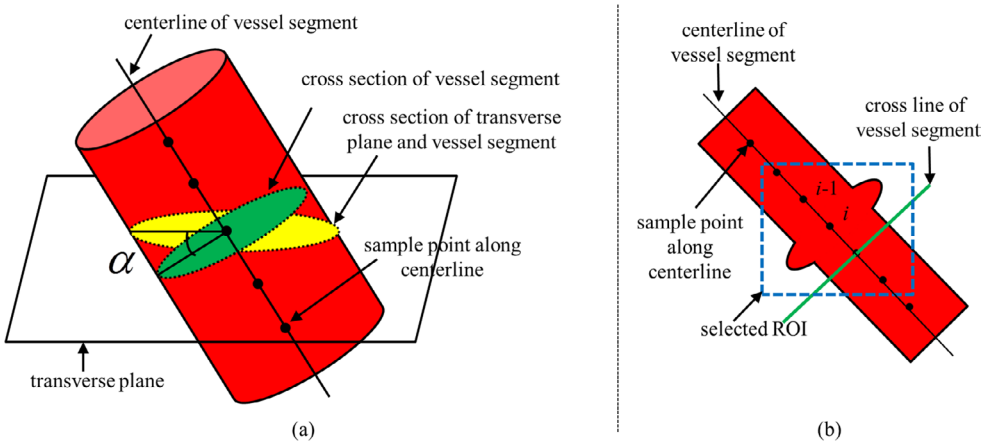

Figure 5. Illustration of our shape consistency check.

cross section should not change drastically. Based on these two rules, we check the candidate set and identify suspicious pixels which could be false positives and false negatives for further verification. Specifically, we first calculate the centreline of the segmented vessel structure based on distance transform and non-maximum suppression (as shown in figures 4(a) and 5). Along the vessel's centreline, we uniformly sample a list of points for shape consistency check (i.e. the diameter or the area of a vessel's cross section should remain similar within a short distance along the vessel's direction). For 3D data, the distance between two sample points is determined based on the thickness between two slices of the CT or MRI scan. At each sample point, we calculate the area of the cross section of the transverse plane and the vessel segment, and the angle between the centreline and the transverse plane (as shown in figure 5(a)). Then the area of the cross section of the vessel segment at the corresponding point can be computed according to equation (10):

$$\text{Area}_{\text{vessel}}(i) = \cos\alpha \times \text{Area}_{\text{Tplane\_vessel}}(i) \tag{10}$$

For each sample point i, we check whether its $\text{Area}_{\text{vessel}}(i)$ is significantly greater or smaller than $\text{Area}_{\text{vessel}}(i-1)$ at its previous sample point $i-1$, i.e. $\|\text{Area}_{\text{vessel}}(i) - \text{Area}_{\text{vessel}}(i-1)\| > \delta$,

where δ is a predefined threshold. Abrupt increase or decrease in a vessel's cross sectional area at sample point i indicates incorrect segmentation containing nearby non-vessel tissues or misdetection of vessel tissues due to poor image quality at slice i (as shown in figure 4(b)). For those cases, we select an ROI encompassing the vessel segments at slice $i-1$ and propagate the location and size of the ROI to the slice i (as denoted by the green rectangle in figure 4(b)). Progressive contrast enhancement is performed within the ROI region, pixel classification based on double thresholding and boundary refinement are then applied to the enhanced ROI region in order to revise the previous segmentation results (as shown in figure 4(c)). If a segmentation that was a single connected component in the original slice i and can be separated in the enhanced image, meanwhile there is one connected component in i having a consistent shape with the previous slice $i-1$, then the remaining connected components are removed as false positives. Once the segmentation result is revised at slice i, it can be further used to guide the shape consistency and connectivity check at sample point $i+1$. This process continues until it reaches the last slice.

Similarly, for 2D data we calculate the centreline of a vessel segment and then at each sample point i we find a cross line which is perpendicular to the centreline passing the sample point and intersects with the two vessel boundaries (as shown in figure 5(b)). Accordingly, the length of the cross line $\mathrm{Len}_{\mathrm{vessel}}(i)$ indicates the diameter at the sample point i. If $\|\mathrm{Len}_{\mathrm{vessel}}(i) - \mathrm{Len}_{\mathrm{vessel}}(i-1) > \delta\|$, where δ is a predefined threshold, an abrupt shape change is detected at sample i, implying potential segmentation errors nearby. Once such a case is detected, we select an ROI encompassing vessel segments which include both sample points i and $i-1$ as well as four extra sample points which are spatially adjacent to i and $i-1$ along the centreline and have a consistent shape (i.e. a similar length of the cross line) with either i or $i-1$ (as shown in figure 5(b)). Afterwards, progressive contrast enhancement is applied to the ROI region, followed by pixel classification and boundary refinement as described above.

The main reason why the segmentation performance can be further enhanced by selecting ROIs around suspicious pixels and performing further enhancement within the selected ROIs is because in the previous progressive contrast enhancement step, the image is partitioned into equal-sized grids without considering the content in each grid (as denoted by yellow grids in figure 4(b)). As a result, it is possible to partition pixels of a vessel into different grids, resulting in degradation of contrast enhancement's performance. By checking the shape consistency and vessel's connectively, we can adjust ROIs so as to encompassing a complete vessel segment and hence yield better enhancement and segmentation.

3. Results

This study, approved by a local institutional review board, consists of evaluation of two 2D datasets and one 3D dataset. The images used for evaluation includes a public 2D retinal dataset named DRIVE (Staal *et al* 2004), a 2D clinical cerebral dataset, and a 3D dataset including 11 clinical CTA cerebral data. In the following, we first describe each of the datasets, the evaluation metric, followed by the results and analysis. In addition, we applied our system to a clinical application—quantitative analysis of cerebral aneurysm development—to demonstrate the effectiveness of our method for real clinical usage.

3.1. Evaluation on 2D datasets

3.1.1. Datasets. We first evaluated our method on a publicly available dataset, called DRIVE (Staal *et al* 2004), which includes 40 2D RGB retinal scans for comparative studies on vessel segmentation in retinal images. The size of each image is 768×584 and each pixel of

the image was represented using 3 colour channels, 8 bits per channel. Each image has two ground-truth segmentations obtained by manual delineation from two experts. Among the 40 images, 20 of them were used for training and the rest were used for testing. We test our approach on the testing images of DRIVE. Figures 7(a) and (b) show an exemplar image and one ground truth image from DRIVE.

In addition to DRIVE, we also examined the performance of our method on two 2D clinical cerebral vessel data. The data was obtained by digital subtraction angiography (DSA), represented using 8 bits grayscale TIFF format. The size of each image is 560×414. For quantitative evaluation, we also asked two experts to manually delineate vessels for each image.

The primary focus of this paper is to improve the segmentation accuracy in two challenging scenarios: (1) regions with low SNRs, and (2) at vessel boundaries disturbed by adjacent non-vessel pixels. Therefore, the ground-truth data should facilitate the evaluation for such challenging cases. To this end, we divided all pixels in each ground-truth image into two parts: (1) easy vessel pixels which can be correctly classified as vessels by both baseline methods, and (2) challenging vessel pixels which are incorrectly labeled as background by at least one baseline method. In this experiment, we implemented a vesselness-based method and an OOF-based method as our baselines (details about the baselines will be elaborated in section 3.1.3). The threshold for binary classification is set to ensure a precision over 95%. Figures 7(c) and (d) illustrate the easy and challenging vessel pixels of a ground truth image of DRIVE, respectively. Obviously, challenging pixels mainly locate around vessel boundaries and at small vessels with very low contrast to its surrounding background.

3.1.2. Evaluation metric. We used the recall-precision curve to evaluate overall segmentation performance on the 2D datasets by varying the threshold parameter for binary classification. As mentioned in section 2.1, we focus our evaluation on challenging pixels, thus we exclude easy vessel pixels from the precision-recall calculation. Specifically, recall is defined as the number of challenging true positives (i.e. challenging pixels which are labeled as vessel pixels in both ground truth and the segmented image) divided by the total number of challenging vessel pixels in the ground-truth. Precision is defined as the number of challenging true positives divided by the total number of challenging pixels that are identified as vessel pixels in the segmented image, as shown in equations (11) and (12),

$$\text{Recall} = \frac{TP - TP_{\text{easy}}}{\text{challenging vessel pixels in ground truth}} \tag{11}$$

$$\text{Precision} = \frac{TP - TP_{\text{easy}}}{\text{challenging vessel pixels in segmented image}} \tag{12}$$

The larger the area under the curve, the better the performance of a method.

3.1.3. Experimental setup. Any existing vessel enhancement method can be used for the first step of our segmentation framework (as shown in the orange block of figure 1). In this study, we experimented with two popular methods, i.e. multi-scale vesselness and multi-scale OOF, which have been widely-recognized for their good performance for vessel segmentation and are open sourced for a fair comparison. We utilized the ITK SDK for the implementation of multi-scale vesselness and the package from Optimally Oriented Flux implementation (2013) for the implementation of OOF. For each filter, we manually tuned parameters to obtain the best performance. Such parameters are then used throughout the entire evaluation process. For both filters, we used identical parameters for multi-scale processing, i.e. the minimum

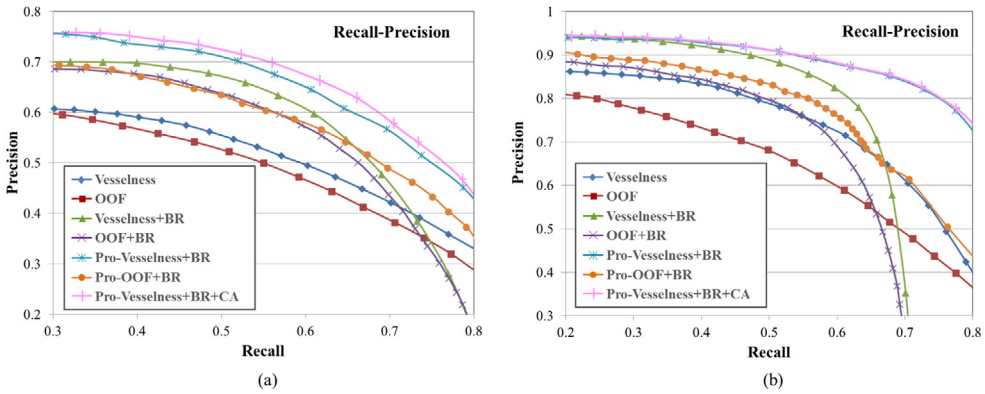

Figure 6. Recall-precision curves obtained for (a) the retinal vessel data and (b) the cerebral vessel data. Experimental results show that our method with the three proposed techniques (i.e. Pro-Vesselness + BR + CA) outperforms all other methods over the entire range. (a) Result comparison on retinal vessel data. (b) Result comparison on cerebral vessel data.

and maximum standard deviations of Gaussian are set to 0.5 and 5, respectively, and the total number of scales is set to 10.

We compared our method, i.e. vesselness with all proposed techniques (Pro-vesselness + BR + CA), with the two baseline methods: vesselness, OOF, as well as four variants of our methods: vesselness with boundary refinement (i.e. vesselness + BR), OOF with boundary refinement (OOF + BR), vesselness with progressive enhancement and boundary refinement (Pro-vesselness + BR), and OOF with progressive enhancement and boundary refinement (Pro-OOF + BR).

3.1.4. Results. Figures 6(a) and (b) show the comparison results on DRIVE and the cerebral data respectively. Three main observations can be made from the results:

(1) By comparing the performance of vesselness (the blue curves) and vesselness + BR (the light green curves) we observe that boundary refinement can greatly improve the precision when the recall is relatively small (i.e. the recall is less than 75% in (a) and less than 70% in (b)). We believe that the performance gain is because our boundary refinement (BR) can effectively remove false positives arising from random noises and the disturbing objects adjacent to vessel boundaries. As the recall increases over a certain point, BR could adversely decrease the precision. We believe the large error is induced by incorrectly-detected edge pixels by canny, including miss detected true edges of vessels and mistakenly detecting edges on noises, especially in regions with low contrast and low SNRs. Incorrect edge pixels may lead to errors in the verification map, yielding incorrect removal of true vessel pixels. As a result, reducing the threshold cannot improve the recall any more while reduce the precision. Similar results can be observed by comparing the results of OOF (the red curves) and OOF + BR (the purple curves) for both datasets.
(2) By comparing the performance of vesselness (the blue curves), vesselness + BR (the light green curves) and Pro-vesselness + BR (the light blue curves), we observe that Pro-vesselness + BR outperforms the other two methods over the entire range. In particular, for large recall (i.e. greater than 70%) progressive contrast enhancement can help greatly boost the precision of vesselness + BR. The result demonstrates the effectiveness of progressive contrast enhancement for improving the contrast and SNR in regions with poor

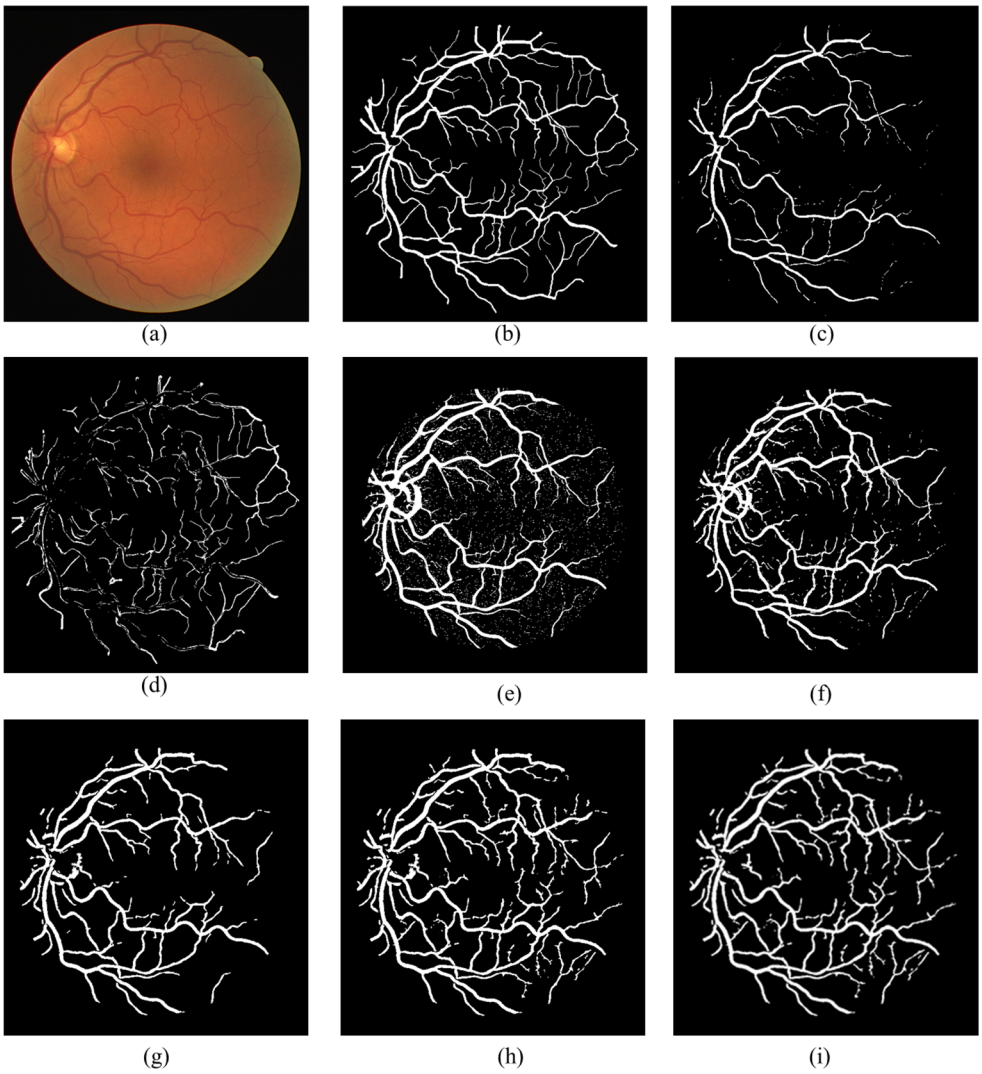

Figure 7. Illustration of segmentation results on an exemplar retinal image. (a) The original image. (b) A ground truth image. (c) and (d) indicate easy and challenging vessel pixels of the ground truth image. (e)–(i) show the segmentation results of four methods in which pro-vesselness + BR achieves the best performance. (a) Original image. (b) Ground truth. (c) Easy vessel pixels. (d) Challenging vessel pixels. (e) Vesselness. Recall: 57.3%, precision: 33%. (f) OOF. Recall: 57.6%, precision: 38%. (g) Vesselness + BR. Recall: 57.3%, precision: 43%. (h) Pro-vesselness + BR. Recall: 72.2%, precision: 41%. (i) Pro-vesselness + BR + CA. Recall: 74.6%, precision: 43%.

quality, which could in turn increase the detection rate of vessels in those regions. Similar results can be also observed for methods based on OOF.

(3) By comparing the performance of Pro-vesselness + BR (the light blue curves) and Pro-vesselness + BR + CA (the pink curves) we observe that for the DRIVE dataset adding content-aware ROI adjustment can further improve the performance. This is because for regions which include small vessels, exudates, and haemorrhage points, adjusting the ROI region so as to exclude the majority of non-vessel pixels can improve the contrast

enhancement performance and meanwhile remove false positives. Therefore, the curve obtained by Pro-vesselness + BR + CA is superior to that achieved by Pro-vesselness + BR. For the cerebral DSA dataset, the two curves almost overlap. This is because DSA images do not highlight bone tissues that are very close to vessels; therefore, little improvement can be obtained by adjusting ROI regions.

Figures 7(e)–(i) show the segmentation results for a retinal image based on different methods. We omit the results for OOF + BR and Pro-OOF + BR as their results are similar to those of vesselness + BR and Pro-vesselness + BR. For vesselness, OOF and vesselness + BR (as shown in figures 7(e)–(g)), we manually tuned the threshold so that the recalls for the three methods are similar (57% $\sim$ 58%). Accordingly, vesselness + BR achieves 10% and 5% greater precision than vesselness and OOF respectively. Further integrating progressive contrast enhancement into the system can improve the recall by another 10% $\sim$ 15% and meanwhile maintain a similar precision (as shown in figure 7(h)). After applying content-aware ROI adjustment, shown in figure 7(i), the recall and precision can be further improved by 2.4% and 2% respectively.

The average runtime of our method for the DRIVE dataset is around 1 to 2 min for each image. The actual runtime depends on the variance of the vessel sizes. If the variance of the sizes among the vessels in a given image is large, more pixels will need contrast enhancement, resulting in longer runtime.

3.2. Evaluation on 3D datasets

3.2.1. Datasets. Our 3D dataset contains 11 CTA images, each of which contains a 3D image volume including both anterior cerebral circulation arteries (ACCA) and posterior cerebral circulation arteries (PCCA). Single aneurysm appears in 9 datasets, one located at the internal carotid artery (ICA), four located at the bifurcation of middle cerebral arteries (MCA) and the other four located at the tip of basilar arteries (BA). The acquisition of data was performed using a 64 detectors scanner with 120 kV/250–300 mA for amplier tube, 0.75 slice collimation and slice spacing of 0.5 mm. A total of 63 ml of non-ionic contrast fluid was intravenously administrated at a rate of 3 ml s^{-1}. The images were reconstructed on a 512×512 volume with a square FOV of 18 cm, yielding an in-plane resolution of 0.35 mm.

3.2.2. Evaluation metric. We evaluated the segmentation accuracy using the Dice similarity coefficient (DSC), a widely used metric to evaluate segmentation algorithms for different medical image modalities. The DSC is defined as:

$$\mathrm{DSC}(S, G) = \frac{2 \times |S \cap G|}{|S| + |G|} \tag{13}$$

where S and G represent the sets of automatically segmented voxels and manually segmented voxels respectively; $|\cdot|$ denotes the set cardinality. The DSC ranges from 0, if S and G do not overlap at all, to 1, if S and G are identical. We compare our method including all three improvements with five baseline methods: the active contour with thresholding method (AC1) and the active contour with clustering method (AC2) (Yushkevich *et al* 2006), efficient flux (Law and Chung 2009), optimally oriented flux (Law and Chung 2008) (OOF), and the thresholding method (Thresholding 2015) (Wang *et al* 2015a). We used the implementation in ITK-SNAP for AC1 and AC2, the source code provided by the original authors for efficient flux and OOF. For Wang *et al* (2015a), we implemented it by ourselves and tried our best to duplicate their performance reported in Wang *et al* (2015a).

Table 1. Comparison of segmentation methods.

Data	Ours	AC1 (Yushkevich *et al* 2006)	AC2 (Yushkevich *et al* 2006)	Efficient flux (Law and Chung 2009)	OOF (Law and Chung 2008)	Thresholding (Wang *et al* 2015a)
1	0.95	0.68	0.65	0.58	0.63	0.58
2	0.93	0.75	0.46	0.76	0.76	0.64
3	0.95	0.69	0.63	0.61	0.60	0.59
4	0.97	0.66	0.49	0.64	0.61	0.58
5	0.89	0.63	0.71	0.64	0.61	0.65
6	0.96	0.78	0.73	0.77	0.79	0.71
7	0.92	0.68	0.47	0.71	0.73	0.62
8	0.91	0.78	0.76	0.65	0.67	0.69
9	0.95	0.72	0.68	0.71	0.73	0.56
10	0.93	0.67	0.46	0.68	0.68	0.60
11	0.93	0.78	0.66	0.68	0.70	0.63
Ave	0.94	0.71	0.61	0.68	0.68	0.62

3.2.3. Results. Table 1 summarizes the average DSC for all the methods. The average DSC achieved by our method is 94% which is 23% $\sim$ 33% greater than the other baseline methods. Figures 8(a)–(g) show segmentation results of an exemplar dataset obtained by different methods. We observe that results of the active contour, efficient flux, OOF and thresholding methods have many false positives at bone tissues since at those regions bone tissues are attached to ICA and have highly similar intensity values as ICA. Active contour with clustering achieves better results at ICA regions than the other four baseline methods; however, the segmented arteries are thinner than the ground truth, which could yield inaccurate measurements of aneurysms in practice. In comparison, our method achieves accurate results for both ICA regions and vessel boundaries.

3.3. Application to cerebral aneurysm development analysis from 3D CTA images

We applied our method to quantitative analysis of cerebral aneurysm development from 3D CTA Images. In the following we briefly present details of methods for aneurysm development analysis, data, followed by results.

3.3.1. Methods. For a patient diagnosed with cerebral aneurysm, a follow-up check was scheduled around six months after the initial CT scan. We segmented vessels as well as aneurysms from these two cerebral CT scans captured at two different times. Then, we registered the two vessel segmentations to quantitatively analyse the development of cerebral aneurysms. Specifically, we utilized registration to align images of cerebral vessels acquired at different times and then we compared the registered images to obtain changes of vascular structures. In principal, aneurysms could grow bigger over time, resulting in differences between the registered images. Normal vessels, on the other hand, remain the same over time and thus yield little changes between corresponding regions on the registered images. By analysing differences between the registered images, we could quantitatively evaluate the development of the aneurysm.

The accuracy of the registration algorithm greatly affects the accuracy of aneurysm development analysis, i.e. misalignment between images results in false alarms at normal vessel regions. There exist many methods for medical image registration. In this experiment, we employed an automatic non-rigid registration method based on mutual information (Yuksel

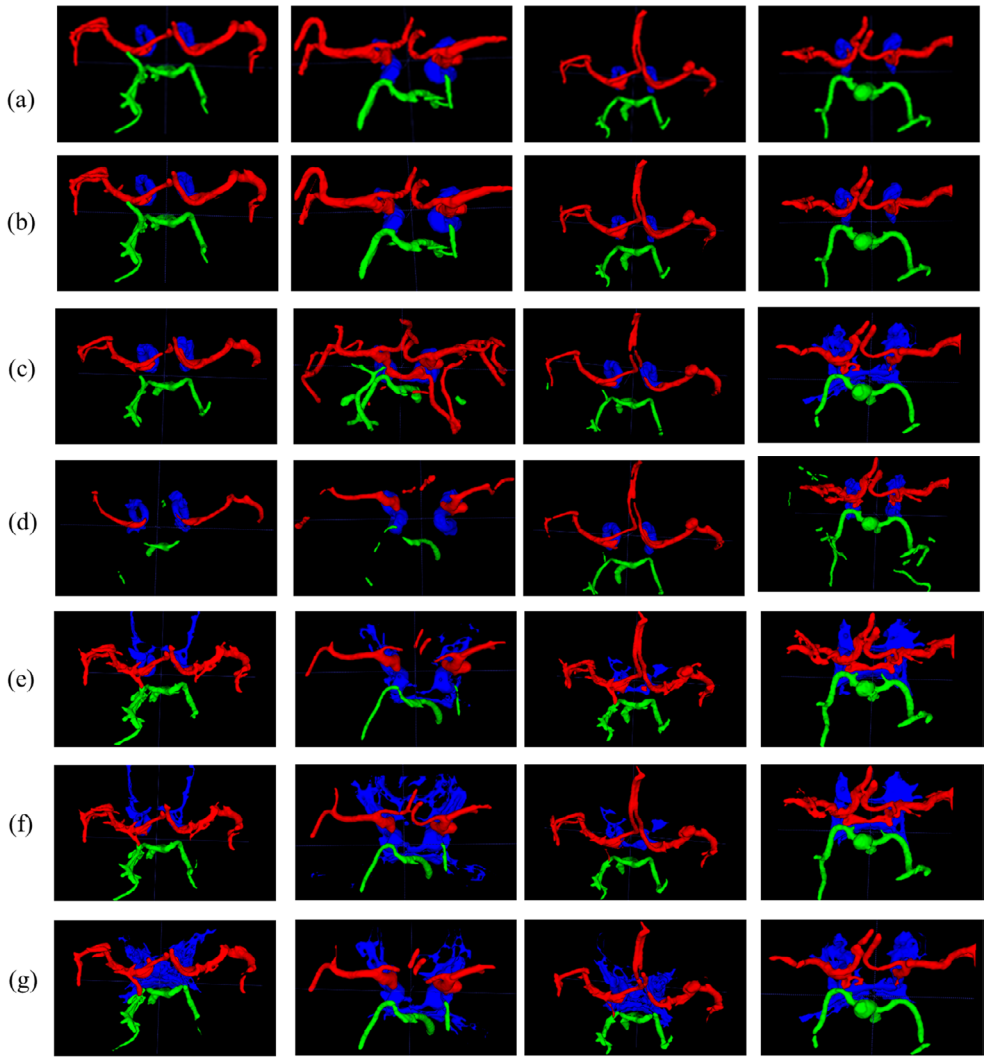

Figure 8. Exemplar segmentation results based on (a) manual segmentation, (b) our method, (c) AC1, (d) AC2, (e) efficient flux, (f) OOF, and (g) Thresholding 2015.

2005). We utilized B-spline basis functions to describe the Free Form Model for the non-rigid registration. The B-spline functions are uniformly placed on a grid of control points. We utilized a 3-level multi-resolution strategy to reduce the computational cost of the non-rigid registration and for each level we set the distance between every two control points to 16.

3.3.2. Datasets. We collected 10 patients' data; each patient has two scans acquired at two distinct time points. An average interval between the two acquisition time points is 126.8 ± 80.1 d. All subjects have a single cerebral aneurysm. Based on radiologists' manual segmentation and measurement, six patients' aneurysms have obvious growth (i.e. indicated as set_grow in tables 2 and 3) and the sizes of the other four patients' aneurysms were known to remain stable between the two time points (i.e. denoted as set_control in tables 2 and 3). All the data are acquired using the same configuration as described in section 3.2.1. To demonstrate that

Table 2. Image characteristic comparison between two images in a set.

Data	Vessel intensity Mean ± S.D.	Non-vessel intensity Mean ± S.D.	#Vessel voxels	#Non-vessel voxels	SNR	Sizes
Set1-grow	1216 ± 70	1107 ± 367	7643	553 9657	1.88	[246,205,110]
Set1-control	1197 ± 60	1068 ± 372	6043	510 9557	2.28	[203,210,120]
Set2-grow	1219 ± 82	1121 ± 196	16 375	741 185	1.68	[118,107,60]
Set2-control	1242 ± 101	1135 ± 485	34 647	471 8553	1.80	[233,204,100]
Set3-grow	1280 ± 120	1073 ± 316	32 618	133 7492	3.53	[161,115,74]
Set3-control	1326 ± 139	1058 ± 230	36 859	124 9285	4.50	[157,128,64]
Set4-grow	1294 ± 135	1066 ± 87	35 493	460 211	3.86	[131,88,43]
Set4-control	1239 ± 99	1066 ± 94	21 530	407 815	2.99	[141,105,29]
Set5-grow	1268 ± 130	1067 ± 386	41 721	540 0149	3.75	[289, 269, 70]
Set5-control	1316 ± 133	1119 ± 395	40 925	525 7225	3.25	[286, 285, 65]
Set6-grow	1215 ± 72	1075 ± 170	24 931	727 445	2.43	[141,116,46]
Set6-control	1157 ± 57	968 ± 253	36 258	788 353	3.15	[151, 127, 43]
Set7-grow	1209 ± 64	1069 ± 423	37 447	101 008 43	2.46	[193,170,114]
Set7-control	1250 ± 52	1090 ± 420	38 166	115 928 94	2.75	[204,181,90]
Set8-grow	1371 ± 146	1101 ± 224	18 471	419 965	4.38	[146,91,33]
Set8-control	1298 ± 79	1099 ± 218	8030	394 054	3.34	[146,102,27]
Set9-grow	1253 ± 111	989 ± 345	31 602	113 4498	4.73	[156,115,65]
Set9-control	1209 ± 84	980 ± 349	22 301	151 9109	4.19	[167,142,65]
Set10-grow	1262 ± 101	1071 ± 112	26 158	400 658	3.28	[114,96,39]
Set10-control	1217 ± 71	1069 ± 87	25 355	454 498	2.58	[131,99,37]

Table 3. Aneurysm development analysis.

Data	Set1-control	Set2-control	Set3-control	Set4-control	Set5-grow	Set6-grow	Set7-grow	Set8-grow	Set9-grow	Set10-grow
Growth rate	0.287%	0.617%	0.335%	0.438%	17.7%	25.7%	31.4%	15.5%	13.4%	10.7%
Avg	0.419 ± 1.46%				19.07 ± 7.91%					

our automatic image segmentation and registration tool is robust to different image qualities, we quantitatively characterize image quality based on the following metrics:

- **Vessel intensity mean and standard deviation (S.D.)** which indicate the average and standard deviation of image intensity inside vessels. The intensity of vessels changes with the amount of contrast agent. In addition, due to inhomogeneity of the contrast agent, the intensity values inside vessels vary as well. Therefore, corresponding vascular pixels in CTA images scanned at different times could have different intensity values. The mean and the S.D. of the vessel intensity can well capture the intensity statistics at vascular locations.
- **Non-vessel intensity mean and standard deviation (S.D.)** which are used to capture the average and the standard deviation of image intensity outside the vessels.
- **Number of vessel pixels and non-vessel pixels** which denote the number pixels inside and outside the vessels respectively.

- **Signal-to-noise ratio (SNR)** which is defined in equation (14) is a widely-used metric to evaluate image quality by comparing the vessel signal and background noises.

$$\mathrm{SNR} = 10 \times \log_{10}\left(\frac{\sum_{i\in \text{vessels}} I(i)^2}{\sum_{i\in \text{ background}} I(i)^2}\right) \tag{14}$$

- **Image size** which denotes the 3-dimensional size of an image.

Table 2 summarizes the characteristics of our data. The datas SNR, the number of non-vessel voxels and the size are quite different both among different patients and between 2 scans of the same patient, indicating different image qualities and different numbers of disturbing voxels in our testing dataset. In addition, for non-vessel voxels we observe that although the average intensity values are similar between two scans of a patient and among different patients' data, the standard deviations are quite large and are different among different data. Large S.D. values yield intensity overlaps with vessel voxels, increasing the difficulty of accurate segmentation.

3.3.3. Results. Table 3 summarizes the growth rate of aneurysm for each dataset. The growth group showed an average $19.07 \pm 7.91\%$ increase in the aneurysm volume, and the non-growth group showed an average $0.419 \pm 1.46\%$ increase in aneurysm volume. The difference in sample means between the growth group and the non-growth group was statistically significant ($p \leqslant 0.05$), i.e. for subjects whose aneurysms grow over time, the growth rate is obviously greater than those whose aneurysms are under control. For all cases, automated diagnosis based on our method is consistent with radiologists' manual diagnosis, demonstrating the potential effectiveness of our system for automated aneurysm development analysis in clinical usage. Running on an Intel Core i7-4600U Processor at 2.7GHz, the average runtime for processing segmentation is 29.6 ± 25.4 s for processing segmentation and 37.9 ± 30.7 s for registration.

4. Conclusion

This paper presents a framework for accurate vessel segmentation in two challenging scenarios: in regions with low intensity contrast and low SNRs, and at vessel boundaries. To this end, we propose and validate three novel techniques: *progressive contrast enhancement*, *boundary refinement* and *content-aware ROI adjustment*. Progressive contrast enhancement iteratively improves visibility of challenging pixels (usually pixels of small vessels and/or at vessel boundaries) which were not distinguishable in previous iterations. By excluding easy vessel pixels which can be labeled with high confidence from further consideration in each iteration, more emphasis are placed on challenging vessel pixels and in turn are much better highlighted by CLAHE-based enhancement. Moreover, progressive contrast enhancement de-emphasizes importance of pixels which are less likely to be vessels according to their shape responses in the enhancement procedure. Due to the complementary information provided by the intensity and the shape, this strategy can effectively suppress noises spread in a homogeneous background. To further reduce false positives around vessel boundaries, we propose boundary refinement which constructs a verification map based on canny edges. Additionally, an equal-sized griding strategy based on a predetermined grid size without considering the content could partition connected vessel pixels into different grids or including non-vessel pixels which have a similar intensity as vessels in the same grid. This partition strategy may greatly limit the amount of improvements achieved by contrast enhancement. To address this problem, we propose a content-aware ROI adjustment method which checks

the shape consistency and continuity of the segmented vessels, and adaptively adjust the locations and sizes of ROIs to contain suspicious pixels which might be incorrectly segmented in previous steps. Experimental results on both 2D and 3D datasets demonstrate that the three proposed techniques can greatly improve the performance of the state-of-the-art segmentation methods. A clinical application of our method—quantitative analysis of cerebral aneurysm development—demonstrates that our system provides consistent diagnosis with clinicians' manual measurement, exhibiting its promising potential for clinical applications.

Acknowledgments

This work was supported by the National Natural Science Foundation of China grant 61502188.

References

Agam G and Wu C 2005 Probabilistic modeling based vessel enhancement in thoracic CT scans *2005 IEEE Computer Society Conf. on Computer Vision and Pattern Recognition* vol 2 pp 649–54 (IEEE)

Annunziata R, Garzelli A, Ballerini L, Mecocci A and Trucco E 2015 Leveraging multiscale hessian-based enhancement with a novel exudate inpainting technique for retinal vessel segmentation *IEEE J. Biomedical Health Inform.* **20** 1129–38

Bauer C and Bischof H 2008 A novel approach for detection of tubular objects and its application to medical image analysis *Joint Pattern Recognition Symp.* pp 163–72

Becker C, Rigamonti R, Lepetit V and Fua P 2013 Supervised feature learning for curvilinear structure segmentation *Int. Conf. on Medical Image Computing and Computer-Assisted Intervention* pp 526–33 (Springer)

Bustamante M, Petersson S, Eriksson J, Alehagen U, Dyverfeldt P, Carlhäll C J and Ebbers T 2015 Atlas-based analysis of 4D flow CMR: automated vessel segmentation and flow quantification *J. Cardiovascular Magn. Reson.* **17** 1

Cabezas M, Oliver A, Lladó X, Freixenet J and Cuadra M B 2011 A review of atlas-based segmentation for magnetic resonance brain images *Comput. Methods Programs Biomed.* **104** e158–77

Canny J 1986 A computational approach to edge detection *IEEE Trans. Pattern Anal. Mach. Intell.* **PAMI-8** 679–98

Frangi A F, Niessen W J, Vincken K L and Viergever M A 1998 Multiscale vessel enhancement filtering *Int. Conf. on Medical Image Computing and Computer-Assisted Intervention* pp 130–7 (Springer)

Fraz M M, Remagnino P, Hoppe A, Uyyanonvara B, Rudnicka A R, Owen C G and Barman S A 2012 Blood vessel segmentation methodologies in retinal images—a survey *Comput. Methods Programs Biomed.* **108** 407–33

Fridman Y, Pizer S M, Aylward S and Bullitt E 2004 Extracting branching tubular object geometry via cores *Med. Image Anal.* **8** 169–76

González G, Fleurety F and Fua P 2009 Learning rotational features for filament detection *IEEE Conf. on Computer Vision and Pattern Recognition* pp 1582–9 (IEEE)

Hernandez M and Frangi A F 2007 Non-parametric geodesic active regions: method and evaluation for cerebral aneurysms segmentation in 3DRA and CTA *Med. Image Anal.* **11** 224–41

Kirbas C and Quek F 2004 A review of vessel extraction techniques and algorithms *ACM Comput. Surv.* **36** 81–121

Lauric A, Miller E, Frisken S and Malek A M 2010 Automated detection of intracranial aneurysms based on parent vessel 3D analysis *Med. Image Anal.* **14** 149–59

Law M W and Chung A C 2008 Three dimensional curvilinear structure detection using optimally oriented flux *European Conf. on Computer Vision* pp 368–82 (Springer)

Law M W and Chung A C 2009 Efficient implementation for spherical flux computation and its application to vascular segmentation *IEEE Trans. Image Process.* **18** 596–612

Nain D, Yezzi A and Turk G 2004 Vessel segmentation using a shape driven flow *Int. Conf. on Medical Image Computing and Computer-Assisted Intervention* pp 51–9 (Springer)

Optimally Oriented Flux implementation 2013 https://github.com/fethallah/ITK-TubularGeodesics

Passat N, Ronse C, Baruthio J, Armspach J P, Maillot C and Jahn C 2005 Region-growing segmentation of brain vessels: an atlas-based automatic approach *J. Magn. Reson. Imaging* **21** 715–25

Pohl K M, Fisher J, Bouix S, Shenton M, McCarley R W, Grimson W E L, Kikinis R and Wells W M 2007 Using the logarithm of odds to define a vector space on probabilistic atlases *Med. Image Anal.* **11** 465–77

Rigamonti R and Lepetit V 2012 Accurate and efficient linear structure segmentation by leveraging ad hoc features with learned filters *Int. Conf. on Medical Image Computing and Computer-Assisted Intervention* pp 189–97 (Springer)

Rigamonti R, Sironi A, Lepetit V and Fua P 2013 Learning separable filters *Proc. of the IEEE Conf. on Computer Vision and Pattern Recognition* pp 2754–61

Roychowdhury S, Koozekanani D D and Parhi K K 2015 Blood vessel segmentation of fundus images by major vessel extraction and subimage classification *IEEE J. Biomed. Health Inform.* **19** 1118–28

Shang Y, Deklerck R, Nyssen E, Markova A, de Mey J, Yang X and Sun K 2011 Vascular active contour for vessel tree segmentation *IEEE Trans. Biomed. Eng.* **58** 1023–32

Staal J, Abràmoff M D, Niemeijer M, Viergever M A and van Ginneken B 2004 Ridge-based vessel segmentation in color images of the retina *IEEE Trans. Med. Imaging* **23** 501–9

Tian Y, Chen Q, Wang W, Peng Y, Wang Q, Duan F, Wu Z and Zhou M 2014 A vessel active contour model for vascular segmentation *Biomed. Res. Int.* **2014** 106490

Volkau I, Zheng W, Baimouratov R, Aziz A and Nowinski W L 2005 Geometric modeling of the human normal cerebral arterial system *IEEE Trans. Med. Imaging* **24** 529–39

Wang R, Li C, Wang J, Wei X, Li Y, Zhu Y and Zhang S 2015a Threshold segmentation algorithm for automatic extraction of cerebral vessels from brain magnetic resonance angiography images *J. Neurosci. Methods* **241** 30–6

Wang S, Yin Y, Cao G, Wei B, Zheng Y and Yang G 2015b Hierarchical retinal blood vessel segmentation based on feature and ensemble learning *Neurocomputing* **149** 708–17

Yang X, Cheng K T T and Chien A 2014 Geodesic active contours with adaptive configuration for cerebral vessel and aneurysm segmentation *ICPR* pp 3209–14

Yu Q, Yang X, Cheng T, Liang F and Chien A 2015 Abstract W MP48: measurement of intracranial aneurysm growth *Stroke* **46** AWMP48

Yuksel S E 2005 Image processing methods for the detection of acute rejection after kidney transplantation *Masters Abstr. Int.* **45** 27–35

Yushkevich P A, Piven J, Hazlett H C, Smith R G, Ho S, Gee J C and Gerig G 2006 User-guided 3D active contour segmentation of anatomical structures: significantly improved efficiency and reliability *Neuroimage* **31** 1116–28

Zhao Y, Rada L, Chen K, Harding S P and Zheng Y 2015 Automated vessel segmentation using infinite perimeter active contour model with hybrid region information with application to retinal images *IEEE Trans. Med. Imaging* **34** 1797–807

Zuiderveld K 1994 Contrast limited adaptive histogram equalization *Graphics Gems* IV (New York: Academic) pp 474–85